Check for updates

Sol–gel synthesis and solar photocatalytic activity of Ca-alloyed ZnO nanoparticles elaborated using different precursors

A. Rosset, [ID] *[ab] K. Djessas, *[ab] V. Goetz,[ab] S. Grillo[ab] and G. Plantard[ab]

Ca-alloyed ZnO nanoparticles elaborated using different calcium precursors ($CaSO_4$, $CaCl_2$, $Ca(NO_3)_2$ and $CaCO_3$) at different [Ca]/[Zn] ratios (0, 1, 5, 10, 15 and 20%) have been prepared by a sol–gel method followed by supercritical drying and annealing at 300 °C. The synthesized samples have been characterized by a number of techniques including Scanning Electron Microscopy (SEM), Transmission Electron Microscopy (TEM), Energy Dispersive X-ray Spectroscopy (EDS), X-ray Diffraction (XRD), Raman Spectroscopy and Electron Paramagnetic Resonance (EPR). SEM and TEM images reveal that the nanoparticles have a quasi-spherical shape with a grain size between 20 and 40 nm. The EDS results on chemical elementary compositions show that the Ca-alloyed ZnO with a $CaCO_3$ precursor and [Ca]/[Zn] ratios of 5 and 10% are quasi-stoichiometric. The XRD results indicate that all the elaborated nanoparticles have a hexagonal wurtzite structure. Using Raman Spectroscopy a supplementary vibrational mode is detected in the case of $CaSO_4$, $CaCO_3$ and $Ca(NO_3)_2$ precursors. The intrinsic defect centers and defect number have been studied using EPR. Two intrinsic defects with different *g* factors are identified by EPR for which the spectral intensities change with calcium precursors. Furthermore, EPR reveals a correlation between the defect number and photocatalytic efficiency. The photocatalytic efficiency of the nanoparticles elaborated with different precursors and compositions has been studied for the solar photocatalytic degradation of pyrimethanil, using a solar simulator. The results show that the nanoparticles of Ca-alloyed ZnO elaborated with a $CaCO_3$ precursor give promising results and enhance the photocatalytic efficiency in the solar field.

1. Introduction

Heterogeneous solar photocatalysis belongs to the family of Advanced Oxidation Processes (AOPs), which are respectful of the environment. This process allows mineralization of a great number of organic pollutants in water thanks to the production of hydroxyl radicals. During the last decade it has attracted considerable attention.[1] Photocatalytic activity occurs when the semi-conductor absorbs a photon with energy equal to or greater than the material's band gap, leading to the formation of electron and hole pairs. These pairs can subsequently migrate to the semiconductor's surface and react with adsorbed molecules to generate such reactive species as H_2O_2, superoxide anion radicals ($\cdot O_2^-$) and hydroxyl radicals ($\cdot OH$).[2,3] These species are very strongly oxidative and highly reactive agents, which can degrade in a non-selective way pollutants until their complete mineralization. The principal function of this process

is to produce as many radicals as possible for a given energy received by the semiconductor. However, some problems remain. They concern low kinetics and low capacity to absorb photons particularly in the UV range, producing a low photocatalytic efficiency for pollutant degradation.

The main problem of the semiconductors studied in the literature for this process is the photo-sensibility to the ultraviolet or near visible irradiation. The UV region that initiates the photocatalytic process accounts for only 5% of the total available solar flux reaching the surface of the earth.[4] This represents a maximal irradiation available for the solar catalytic process of $50 \text{ W}_{UV} \text{ m}^{-2}$. Moreover, the overall photocatalytic efficiency obtained with the semiconductors most widely used as catalysts in the literature are relatively weak, of the order of a few percent.[5,6] In this context, it is very important to use efficiently the sunlight in its totality. By contrast, photocatalytic capacities under UV irradiation are higher than those under solar irradiation: a factor of 10 is observed between these two irradiations spectral range. The principal catalysts used in the literature are effective in the UV range but their yield is very low for solar applications.[7–9] Therefore, the objective is either to enhance photocatalytic efficiency in the UV range by restricting the recombination process, or to increase photons usable for

[a]Laboratoire Procédés Matériaux et Energie Solaire, PROMES-CNRS, Rambla de la Thermodynamique, Technosud, 66100 Perpignan Cedex, France. E-mail: aurelie.rosset0868@gmail.com; djessas@univ-perp.fr

[b]Université de Perpignan Via Domitia, 52 avenue Paul Alduy, 66860, Perpignan Cedex 9, France

producing radicals by employing catalysts photosensitive to the visible light. The electron–hole recombination pairs and low photocatalytic efficiency in the photocatalytic reactions hinder the process of photocatalytic degradation. Different methods have been studied in the literature to help decrease the electron–hole recombination rate and/or increase the photocatalytic efficiency of photocatalysts.[2,3,5,10] The development of innovative nanocatalysts, which are effective in the exploitation of solar radiation is therefore a major challenge.

At present, various metal oxide catalysts, such as WO_3, ZnS, SnO_2 and CdS[11–14] are limited in their application by various constraints, *e.g.* toxicity, chemical instability and/or electron–hole recombination. The two main catalysts that have been widely reported in the literature are ZnO and TiO_2.[15–17] ZnO is a promising catalyst for the photocatalytic process due to its photosensitivity, its strong oxidizing capacity, its non-toxicity, its large band gap of 3.37 eV and its excellent chemical and mechanical stability.[18,19] However, ZnO has several weaknesses, such as the fast recombination rate of the photo-generated electrons and holes and a low efficiency in photocatalytic reactions, which obstruct the photocatalytic degradation mechanism.[2,20] To address these limitations, modifications of the ZnO structure by doping and/or alloying with different elements have been proposed to improve the photocatalytic activity. ZnO is doped and/or alloyed with many elements, such as Ce,[8] Mg,[9] Al,[21] I,[22] and Cu.[23] In recent years, the doping and/or alloying of ZnO with transition metals,[24,25] alkaline-earth metals[26] and alkaline metals[25,27] showed that it is possible to increase the photocatalytic activity under visible light and full solar light irradiation, introducing additional energy levels in the band gap of ZnO and thus modifying its electrical and optical properties.[28,29] It has also been demonstrated that the doping enhances the charge separation between the photo-generated electrons and holes, decreases the recombination of electron–hole pairs and lengthens the lifetime of electrons and holes.[19,30] These parameters are directly responsible for photocatalytic efficiency. Among the different alloys commonly studied in the literature, little attention has been devoted to studying the effect of calcium as a dopant or alloying element of ZnO on its photocatalytic activity under solar irradiation.

The present study is focused on the synthesis and characterization of Ca-alloyed ZnO elaborated using different calcium precursors ($CaSO_4$, $CaCl_2$, $Ca(NO_3)_2$ and $CaCO_3$) at different molar ratios to enhance the photocatalytic efficiency. All these catalysts are synthesized by a single sol–gel process.[31] The structural and morphological properties of samples have been investigated by means of Scanning Electron Microscopy (SEM), Transmission Electron Microscopy (TEM), Energy Dispersive X-ray Spectrum (EDS), X-ray Diffraction (XRD), Raman Spectroscopy and Electron Paramagnetic Resonance (EPR). The photocatalytic degradation of pyrimethanil has been studied to evaluate the influence of precursors and the composition of the samples on the photocatalytic activities under solar irradiation. This allows the photocatalytic efficiency under solar irradiation (computed as the number of degraded molecules divided by the effective photons absorbed available for the photocatalytic reaction) to be determined.

2. Experimental

The chemical reagents used in this work are zinc acetate dehydrate [$Zn(OOCCH_3)_2 \cdot 2H_2O$], ethanol ($C_2H_5OH$), methanol ($CH_3OH$), calcium sulfate ($CaSO_4$) or calcium chloride ($CaCl_2$) or calcium carbonate ($CaCO_3$) or calcium nitrate ($Ca(NO_3)_2$). All of these reagents are purchased from Aldrich Chemical Company and are used without further purification.

2.1. Synthesis of Ca-alloyed ZnO

Calcium alloyed ZnO with a calcium sulfate precursor is prepared by sol–gel method using supercritical drying. In a typical preparation procedure, 16 g of zinc acetate dehydrate is first dissolved in 112 ml of methanol under continuous stirring for 15 min at room temperature. An adequate quantity of calcium sulfate, corresponding to [Ca]/[Zn] atomic ratios of 0, 0.01, 0.05, 0.10, 0.15 and 0.20 is added. After 5 min under magnetic stirring, the solution is placed in an autoclave of 1 l capacity to realize the drying under supercritical conditions for ethanol ($T_c = 516$ K, $P_c = 63.3$ bars). Then, the obtained nanoparticles are heated in a furnace in air at 573 K for 2 hours to enhance the powder crystallinity. Nanoparticles of undoped ZnO and $Zn_{1-x}Ca_xO$ elaborated with the three other precursors are also prepared following the same procedure.

2.2. Characterization

The morphology of the $Zn_{1-x}Ca_xO$ nanoparticles elaborated with different calcium precursors has been firstly observed using SEM (model SEM-FEG, Hitachi S-4500) and TEM (model JEM-100CX) operating at an acceleration voltage of 100 kV. The identification of chemical elements in the nanopowders has been performed by EDS (model EDS KEVEX Si(Li) assisted software Brüker). The structural properties of samples has then been investigated by XRD with an X'pert powders Philips diffractometer, using the Cu-Kα radiation ($\lambda = 1.5418$ Å). The diffractograms have been collected at 2θ in the range of 10° to 70° with 0.02° step. The crystallite size has been determined from XRD data using the Debye–Scherrer's formula. The formation of the ZnO phase has been confirmed by Raman spectroscopy measurements using a Horiba Jobin Yvon-LabRAM ARAMIS spectrophotometer equipped with diode laser ($\lambda = 473$ nm) and with power fixed at 16 mW. The EPR method has been used to characterize paramagnetic defects. All EPR measurements have been carried out using a Bruker EMX X-band EPR spectrometer equipped with a 9.8 GHz field modulation unit at room temperature. The resonance has been optimized for the amplitude modulation, frequency modulation, gain, microwave power, time-constant and time conversion. The amount of powder used for all measurements was the same. Additionally, a standard field marker (diphenylpicrylhydrazyl: DPPH polycrystalline with $g = 2.0036$) has been used for the calibration of the resonance magnetic field values and the determination of the exact g-factor of the resonance lines. The shape and area of the EPR spectra have been analyzed using standard numerical methods.
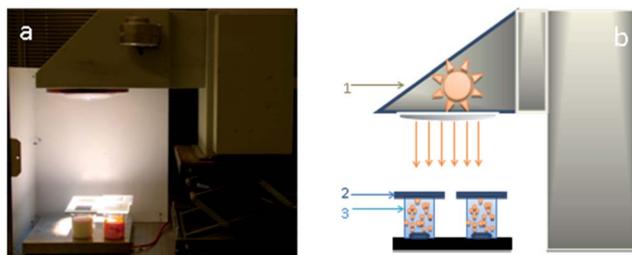
Fig. 1 (a) Photograph of the experimental set-up and solar simulator and (b) experimental set-up for the measurement of pyrimethanil degradation kinetic equipped with a source simulating solar irradiation (1), glass optical filters (Edmond Optics filters) (2), four tank reactors (volume of 0.25 l, irradiated surface of 0.0025 m^2) containing the suspension of catalysts (3).

2.3. Photocatalytic efficiency

A measuring bench has been set-up to evaluate the number of molecules degraded by the nanocatalysts under different irradiation conditions. This bench comprised a solar source, optical filters to control the spectral range applied and a reactor containing the catalyst suspensions (Fig. 1). The solar source is made up of a Newport/Oriel solar simulator of 1000 W m^{-2} power and an AM1.5 solar spectrum. To assess to the real number of photons available for photodegradation of the catalysts on different spectral fields, optical filters provided by Edmund Optics are placed between the solar simulator and the beaker with suspensions (Fig. 1b). The three filters used allow to

work either in the ultraviolet spectral range from 250 to 400 nm with a power of 46 W m^{-2}, or in the visible spectral range from 400 to 560 nm with a power of 315 W m^{-2}, or else with a power of 408 W m^{-2} in the solar range from 250 to 560 nm. The reactor is a set of four beakers of 0.25 l volume containing the target molecule to degrade and 0.3 g of nanocatalyst suspensions under magnetic stirring. Defining in a previous work, a optimal catalyst concentration of 0.3 g l^{-1} is chosen for all experiments.[32] The irradiated surface is 0.0025 m^2. From this configuration, the photocatalytic efficiency of different nanocatalysts is measured and compared under controlled irradiation conditions. The target molecules selected to evaluate the photocatalytic activity of nanocatalysts is pyrimethanil which is present as a residue in water and food and is toxic to human and aquatic life.[33,34] Pyrimethanil belongs to the aniline–pyrimidine class of fungicides and has been used worldwide before harvest for foliar application or post-harvest for fruits treatment.[35] It is used to cure diseases caused by Botrytis, Monilinia, *Venturia pyrina* and other pathogens. Pyrimethanil is not considered readily biodegradable because its half-life is estimated at 8.9–21 days in water. The pyrimethanil and byproducts coming from degradation of the target molecule are tracked by UV-vis spectrophotometer (Thermo scientific evolution 600 UV-vis) using an absorption wavelength of 265 nm. The measurement of degradation kinetics was carried out at an initial concentration of 12 mg l^{-1}. Each sample is filtered and measured in a quartz tank with an optical length of 10 mm.
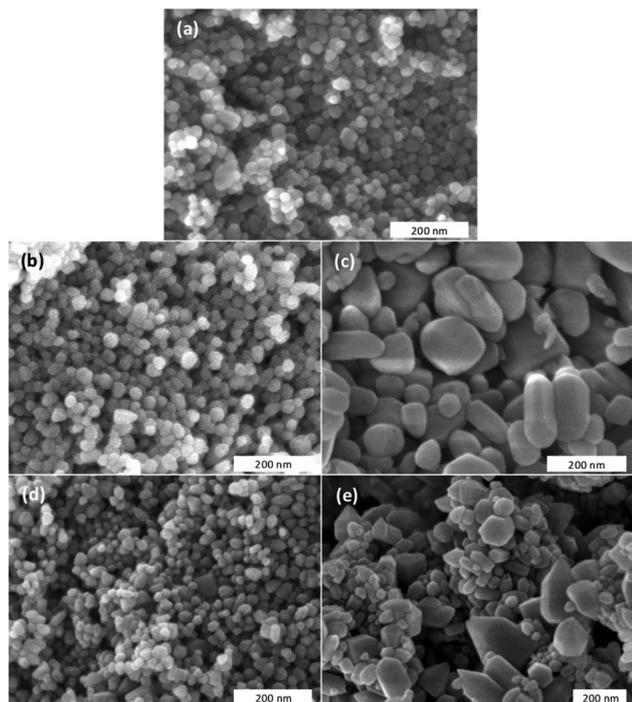

Fig. 2 Scanning electron microscopy images of differently elaborated catalysts calcined in air at 573 K (a) undoped ZnO, (b) $Zn_{0.90}Ca_{0.10}O$ with a $CaSO_4$ precursor, (c) $Zn_{0.90}Ca_{0.10}O$ with a $Ca(NO_3)_2$ precursor, (d) $Zn_{0.90}Ca_{0.10}O$ with a $CaCO_3$ precursor and (e) $Zn_{0.90}Ca_{0.10}O$ with a $CaCl_2$ precursor.
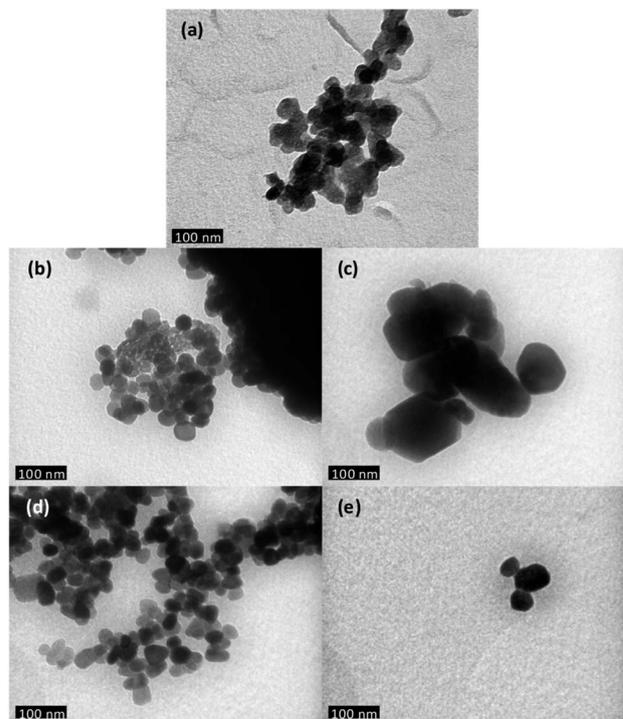

Fig. 3 Transmission electron microscopy images of different catalysts elaborated by sol−gel method and calcined in air at 573 K (a) undoped ZnO (b) $Zn_{0.90}Ca_{0.10}O$ with a $CaSO_4$ precursor, (c) $Zn_{0.90}Ca_{0.10}O$ with a $Ca(NO_3)_2$ precursor, (d) $Zn_{0.90}Ca_{0.10}O$ with a $CaCO_3$ precursor and (e) $Zn_{0.90}Ca_{0.10}O$ with a $CaCl_2$ precursor.

Tests are repeated to ensure the results repeatability, hence all the photocatalytic results presented in this work are the mean of three replicates for each samples. Photocatalytic efficiency is used to discuss and explain the obtained results. The efficiency is the variation in the number of photoconverted molecules as the number of accumulated photons received at the photo reactor surface. A previous study[32] has shown the quantity of adsorbed molecules onto the catalyst is negligible and on other hand, the photolysis can be negligible compared to photo-catalytic mechanism.

3. Results and discussion

3.1. Characterization of the photocatalyst

The morphology and the size of the undoped ZnO and of the $Zn_{1-x}Ca_xO$ nanoparticles have been investigated by SEM. Due to the similarities in terms of size and shape between all calcium contents, authors decided to show only $x = 10\%$. Fig. 2 show SEM images of undoped ZnO and Ca-alloyed ZnO catalysts elaborated with the four precursors ($CaSO_4$, $CaCl_2$, $Ca(NO_3)_2$ and $CaCO_3$) for a calcium contents of $x = 0.10$ and calcined in

air at 573 K. Fig. 2a, b and d show that undoped ZnO and $Zn_{0.90}Ca_{0.10}O$ nanoparticles elaborated with a $CaSO_4$ and a $CaCO_3$ precursors respectively, exhibit mainly quasi-spherical crystallites shapes, with a particle size distribution relatively low and homogeneous centered at 30 nm. The size of these samples is estimated in the range of 20–40 nm. It should be noted that the crystallites size obtained with a $CaCO_3$ precursor is lower than the one of ZnO nanoparticles. Also, it can be seen in Fig. 2c and e that the $Zn_{0.90}Ca_{0.10}O$ nanoparticles prepared with a $Ca(NO_3)_2$ and $CaCl_2$ precursor respectively have hexagonal or spherical shapes. These two SEM images show also the presence of hexagonal sticks shape. These particles have a size, which varies from 20 to 200 nm. It is important to note that the shape and crystallite size of the particles depend on the nature of precursors used during elaboration.

TEM has been performed in order to further carry out the analysis of the crystallites size and morphology. The observation of undoped ZnO and $Zn_{1-x}Ca_xO$ nanoparticles elaborated with a $CaSO_4$, a $CaCl_2$, a $Ca(NO_3)_2$ and a $CaCO_3$ precursor with x at 0.10 is presented in Fig. 3. The undoped ZnO and the $Zn_{0.90}Ca_{0.10}O$ nanoparticles with a $CaSO_4$ and a $CaCO_3$
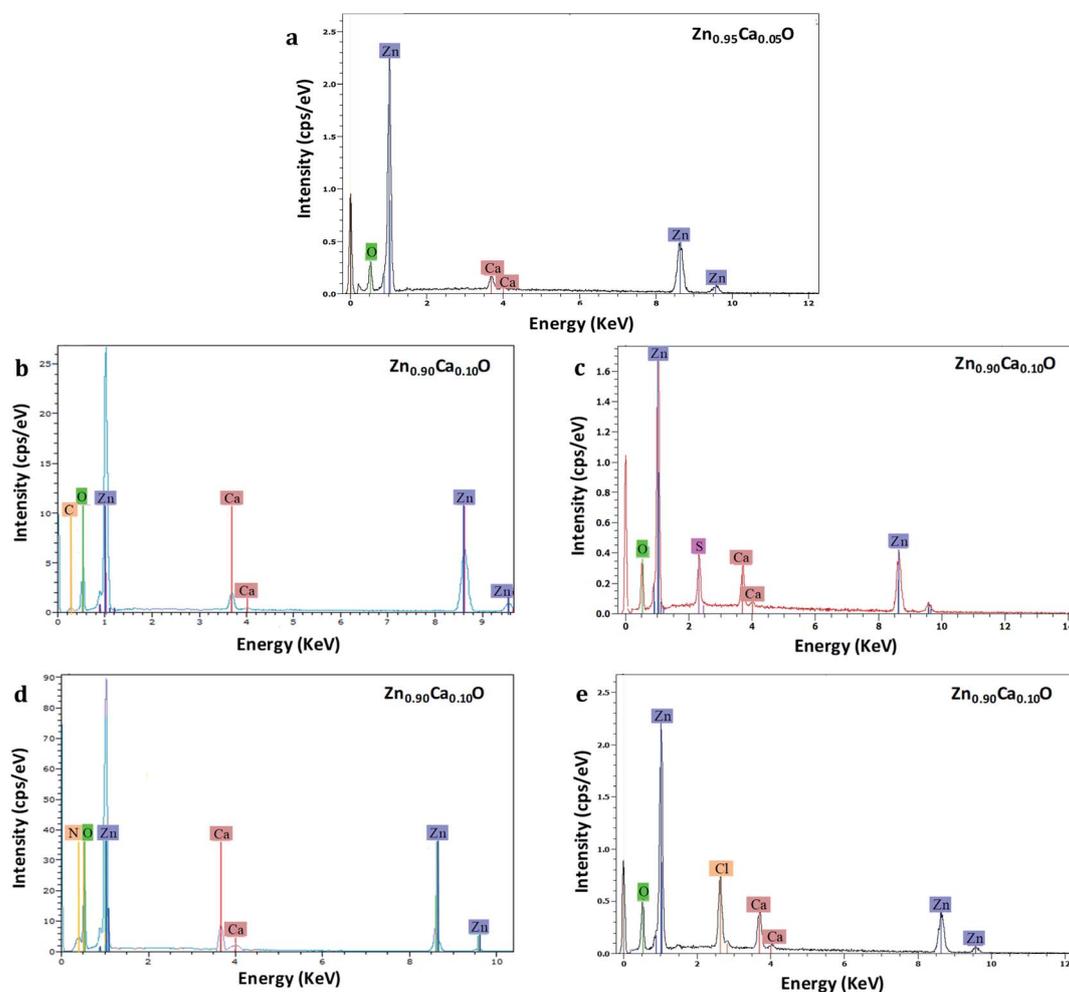

Fig. 4 EDS spectra of $Zn_{0.95}Ca_{0.05}O$ nanoparticles elaborated with $CaCO_3$ precursor (a) and $Zn_{0.90}Ca_{0.10}O$ nanoparticles elaborated from $CaCO_3$ (b), $CaSO_4$ (c), $Ca(NO_3)_2$ (d) and $CaCl_2$ (e) precursors. The nanoparticles are calcined in air at 573 K.

Table 1 EDS results of $Zn_{1-x}Ca_xO$ nanoparticles elaborated with the four precursors at different calcium content

Catalyst	Precursor	[Ca]/[Zn]	Zinc (at%)	Oxygen (at%)	Calcium and other elements (at%)
$Zn_{0.95}Ca_{0.05}O$	$CaCO_3$	0.05	47.02	50.37	Ca: 2.61
$Zn_{0.90}Ca_{0.10}O$	$CaCO_3$	0.10	44.27	50.25	Ca: 4.44 C: 1.04
	$CaSO_4$	0.10	44.08	44.47	Ca: 5.55 S: 5.90
	$CaCl_2$	0.10	26.65	51.56	Ca: 8.34 Cl: 13.45
	$Ca(NO_3)_2$	0.10	50.06	40.08	Ca: 5.10 N: 4.76

precursor, shown respectively in Fig. 3a, b and d, have a quasi-spherical morphology with an average size between 20 and 40 nm. In contrast, for other precursors in Fig. 3c and e, a quasi-spherical, stick or even hexagonal shapes are present. The average nanoparticles size varies from 30 to 200 nm. These

results again confirm that the nature of the precursor used during the synthesis have an influence on nanoparticles size and shape in agreement with those obtained by SEM.

EDS analysis has been performed to measure the chemical compositions of $Zn_{1-x}Ca_xO$ nanoparticles elaborated with
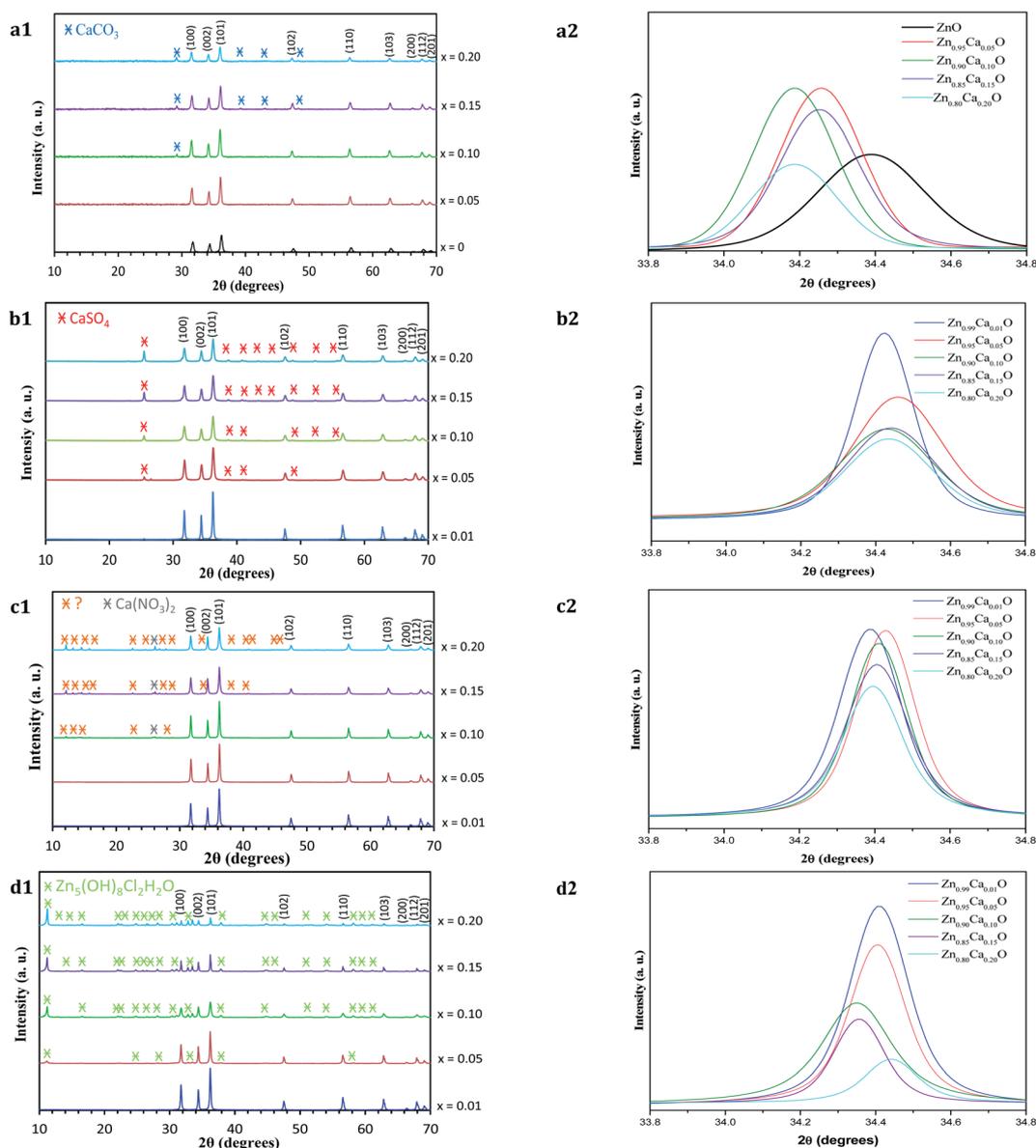

Fig. 5 (1) XRD patterns and (2) their corresponding zoom in on the (002) diffraction peak of $Zn_{1-x}Ca_xO$ nanoparticles elaborated with the four different precursors at different calcium content ($x = 0$ and $0.01 \leq x \leq 0.20$) and calcined in air at 573 K: (a) $CaCO_3$, (b) $CaSO_4$, (c) $Ca(NO_3)_2$ and (d) $CaCl_2$ precursors. The XRD pattern of undoped ZnO nanoparticles is also shown.

different precursors with x varying from 0 to 0.20. This analysis was replicated three times at three different locations on each samples. Fig. 4 shows the EDS spectra of the $Zn_{1-x}Ca_xO$ nanoparticles. EDS confirms the presence of zinc, calcium, oxygen and another element. The peaks observed at 0.5, 1.0 and 3.7 keV are due to the presence of O, Zn and Ca respectively.

However, for the $Zn_{0.90}Ca_{0.10}O$ nanoparticles elaborated with $CaSO_4$, $CaCl_2$, $Ca(NO_3)_2$ and $CaCO_3$ precursors, supplementary elements identified as sulphur, chlorine, nitrogen and carbon are attributed to their respective precursors. Furthermore, for the $Zn_{0.95}Ca_{0.05}O$ nanoparticles elaborated with the $CaSO_4$ precursor, no carbon from the precursor is found. The most relevant results are summarized in Table 1 for calcium contents of 5% and 10%. The elemental composition values for $Zn_{1-x}Ca_xO$ nanoparticles at $x = 0.10$ elaborated with a $CaSO_4$ precursor show that stoichiometry is not respected. In contrast, the quantity of calcium present in the samples is in agreement with the initial content of 10% at $\pm 1\%$, representing the instrumental error. However, the atomic percentage of sulfur and calcium are the same. In this case, the presence of sulfur indicates probably that calcium is not fully inserted in the ZnO matrix. It can be seen from Table 1 that the $Zn_{1-x}Ca_xO$ sample with $x = 0.10$ elaborated with a $CaCl_2$ precursor is not stoichiometric. A significant presence of chlorine and calcium is observed, as well as a high deficiency in zinc. The elemental compositions values obtained for the $Zn_{0.90}Ca_{0.10}O$ nanoparticles elaborated with a $Ca(NO_3)_2$ precursor also show a non-respect of the stoichiometry. This is due to the presence of the nitrogen element in the elaborated catalyst. In contrast, the elemental chemical compositions obtained for the $Zn_{1-x}Ca_xO$ nanoparticles with $x = 0.05$ and $x = 0.10$ elaborated with a $CaCO_3$ precursor are quasi-stoichiometric. The atomic percentage of calcium is in agreement with the elaboration conditions of 5% and 10% at $\pm 1\%$. Moreover, a low presence of carbon is observed for $x = 0.10$. This confirms the presence of calcium in the ZnO matrix. It is important to note that the precursor plays a role on the stoichiometry and on the insertion in the ZnO matrix.

The structure of the undoped ZnO and $Zn_{1-x}Ca_xO$ samples elaborated with different precursors ($CaSO_4$, $CaCl_2$, $Ca(NO_3)_2$ and $CaCO_3$) at different contents has been investigated using X-ray powder diffraction. The XRD patterns of $Zn_{1-x}Ca_xO$ nanoparticles for a number of x values between 0 and 0.20 are shown in Fig. 5.

For all the samples, the positions and relative intensities of the diffraction peaks are in good agreement with powder diffraction standards data (JCPDS no. 36-1451), corresponding to the hexagonal wurtzite structure of ZnO (space group $P6_3mc$) with lattice constants of $a = b = 3.25$ Å, $c = 5.207$ Å. The main peaks are identified as (100), (002), (101), (102), (110), (103), (200), (112) and (201) reflexion planes of ZnO, respectively. For our samples, the (002) diffraction line is narrower than the (101) and (100) lines. This indicates that the crystalline shape is asymmetrical. When the calcium content increases in the ZnO matrix, the degree of crystallinity of the nanoparticles decreases. Indeed, at $x \geq 0.10$ in the case of the $CaCO_3$ and $Ca(NO_3)_2$ precursors and $x \geq 0.05$ with the $CaSO_4$ and $CaCl_2$

precursors, other peaks which do not belong to the wurtzite structure begin to appear. The relative intensity and number of these peaks increases with calcium content. On Fig. 5a1, c1 and b1, the appearance of the secondary phases for $Zn_{1-x}Ca_xO$ when $x \geq 0.10$ with the $CaCO_3$ and $Ca(NO_3)_2$ precursors and $x \geq 0.05$ with the $CaSO_4$ precursor can be attributed to the presence of the precursor itself.[36–38] This is probably due to the limited solubility of the calcium atoms substituting the Zn interstitial sites of the ZnO matrix. In contrast, the secondary phases observed in Fig. 5d1 are identified using the JCPSD 07-0155 database[39,40] and attributed to zinc hydroxyl compound $Zn_5(OH)_8Cl_2–H_2O$. It is formed from a chemical reaction between the zinc and calcium ($CaCl_2$) precursor during the catalyst synthesis. However, the phases presented in Fig. 5c1 are not referenced in the literature.

Furthermore, the lattice parameters $a = b$ and c determined from the positions of the (001) and (002) diffraction peaks for the $Zn_{1-x}Ca_xO$ ($0.01 \leq x \leq 0.20$) elaborated with the $CaSO_4$, $CaCl_2$ and $Ca(NO_3)_2$ precursors are relatively close to those of ZnO. Only with a $CaCO_3$ precursor, an increase of lattice parameters is observed. This is due to the insertion of calcium in the ZnO matrix. In fact, since the atomic radius size of the calcium ion (1.94 Å) is larger than that of the zinc ion (1.42 Å), dislocations appeared and led to a local distortion of the lattice parameter.[41] No modification of the ZnO wurtzite structure is generated.

Nevertheless, the enlargement of (002) diffraction peak is showed in Fig. 5a2 for $Zn_{1-x}Ca_xO$ ($x = 0$ and $0.05 \leq x \leq 0.20$). Only in the case of $CaCO_3$, a shift toward a lower 2θ degrees is observed when the Ca content increases. This shift indicates that the Ca^{2+} ions substituted the zinc sites along the c-axis without modification of the ZnO wurtzite lattice.[42–44] In contrast, on Fig. 5b2–d2 which represent respectively $Zn_{1-x}Ca_xO$ ($0.01 \leq x \leq 0.20$) elaborated with the $CaSO_4$, $Ca(NO_3)_2$ and $CaCl_2$ precursors, the shift of the (002) diffraction peak is relatively low. This indicates that calcium isn't fully integrated into the ZnO matrix. All these results are in agreement with the ones obtained by EDS and presented above. It is important to note that the precursor plays a role on the insertion in the ZnO matrix.

The average crystallite size G of the different samples has been calculated using Debye–Scherrer's formula given in eqn (1).[45]

$$G = \frac{0.9\lambda}{B \cos\theta_B} \tag{1}$$

where λ is the X-ray wavelength (1.5418 Å), B is the line width at half maximum (FWHM) of the XRD peak and θ_B is the Bragg diffraction angle. The average crystallite size obtained for $Zn_{1-x}Ca_xO$ ($0.05 \leq x \leq 0.20$) samples elaborated with the $CaSO_4$ and $CaCO_3$ precursors varies from 22 to 34 nm and is 25 nm for the undoped ZnO. In these two cases, it is interesting to note that the presence of precursors does not influence the crystallites size. In contrast, the average crystallite size for $Zn_{1-x}Ca_xO$ ($0.01 \leq x \leq 0.20$) elaborated with the two other precursors varies from 39 to 56 nm. The crystallite size is much greater compared to that of undoped ZnO. Therefore, the nanoparticles size

variation is directly influenced by the precursor chosen during their synthesis. These results are in good agreements with the crystallites size determined by SEM and TEM.

Raman analysis has been performed to further obtain more information on the structural compositions of the undoped ZnO and $Zn_{1-x}Ca_xO$ nanoparticles elaborated with different precursors ($CaSO_4$, $CaCO_3$, $Ca(NO_3)_2$ and $CaCl_2$) at different calcium contents ranging from $x = 0$ to $x = 0.20$. Raman spectra have been acquired at room temperature and are represented as a function of the wavenumber in the range of 200–1000 cm^{-1} in Fig. 6. The several peaks shown at 331, 382, 415, 437, 574 and 584 cm^{-1} are attributed to the optical phonon of ZnO.[46–48] While the 331 cm^{-1} and 382 cm^{-1} peaks correspond to the second order Raman (multiple phonon processes) E_2 (high)-E_2 (low) and A_1 (TO) modes respectively. The intense peak at around 437 cm^{-1} is assigned to the high frequency branch of the E_2 (high) vibrational mode. This mode corresponds to oxygen motion and is a characteristic of the hexagonal wurtzite phase of ZnO.[49]

Modes are identified for a calcium content of $x = 0.10$, except for the $Zn_{1-x}Ca_xO$ elaborated with the $CaSO_4$ and $CaCl_2$ precursors where the content is $x = 0.05$. The $Zn_{1-x}Ca_xO$ elaborated with the $CaSO_4$, $CaCO_3$ and $Ca(NO_3)_2$ precursors, presented supplementary vibrational modes attributed to the calcium precursor used during the sol–gel synthesis.[37,52,53]

Moreover, the crystallinity of the nanoparticles is directly correlated to the intensity and width of E_2(high) mode.[50] In Fig. 6a, Fig. 6c and Fig. 6b, Ca-alloyed ZnO with a calcium content $x > 0.10$ for the $CaCO_3$ and $Ca(NO_3)_2$ precursors and $x > 0.05$ for the $CaSO_4$ precursor respectively, an intensity decrease of the E_2(high) peak is observed. In the case of the $CaCl_2$ precursor (Fig. 6d), this appear for a calcium content $x > 0.15$. This indicates a degradation of the material's crystallinity. The peak at 584 cm^{-1} attributed at E_1(LO) appears for $x \geq 0.10$. This vibrational mode implies the presence of structural defects assigned to the oxygen vacancies, Zn interstitials and also impurities.[51] Furthermore, the supplementary vibrational the sol–gel synthesis.[37,52,53] Furthermore, the vibrational modes presented in Fig. 6c at 951 and 961 cm^{-1} for this precursor are not referenced in the literature. On the other hand, the supplementary vibrational modes for the $CaCl_2$ precursor are attributed to the zinc hydroxyl compound $Zn_5(OH)_8Cl_2$–H_2O.[54–56] These results are in a perfect agreement with the one obtained by XRD.

3.2. Photocatalytic efficiency

Most studies in the literature are performed under UV irradiation, which is not representative of real solar irradiation.[57,58] Thus, in order to achieve representativeness of the real conditions, the set-up including UV and visible irradiation described above in paragraph 2.3 has used. The objective of this study is to define the photocatalytic performances of nanocatalysts under solar irradiation and to compare them in terms of their photocatalytic efficiency. In the heterogeneous photocatalysis
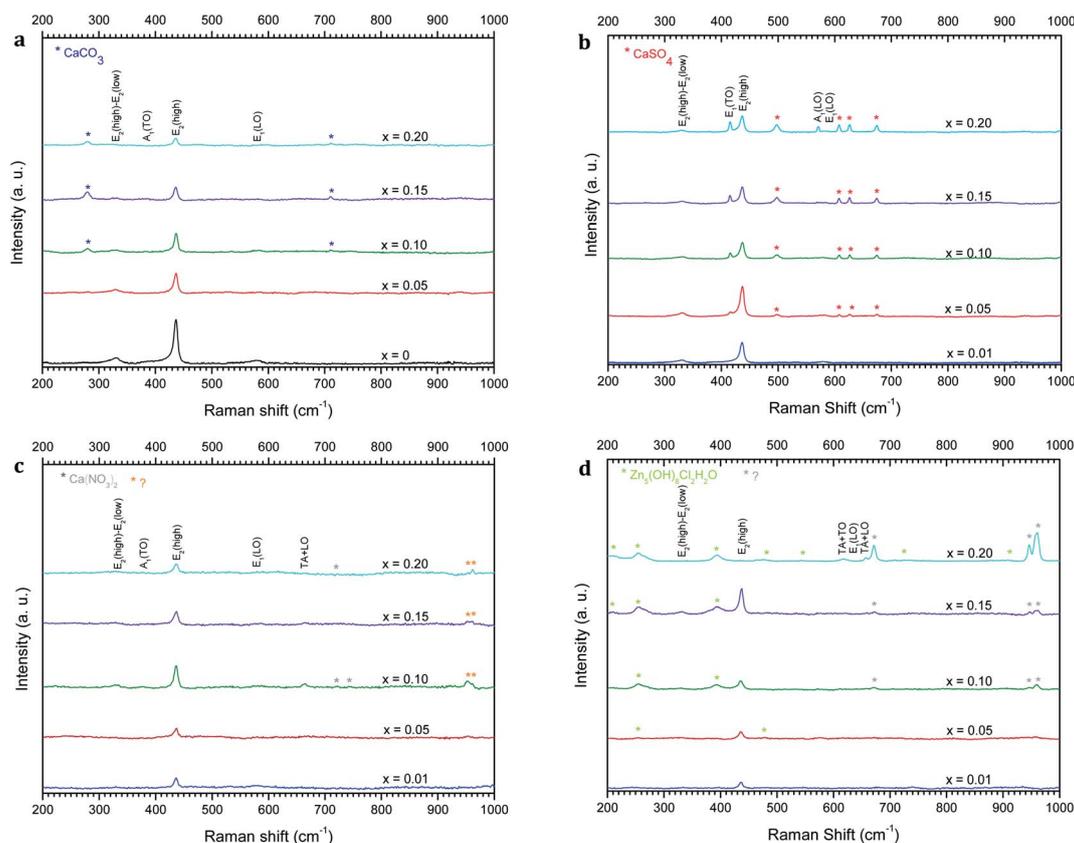

Fig. 6 Raman spectra of $Zn_{1-x}Ca_xO$ ($x = 0$ and $0.01 \leq x \leq 0.20$) nanoparticles elaborated from $CaCO_3$ (a), $CaSO_4$ (b), $Ca(NO_3)_2$ (c) and $CaCl_2$ (d) precursors. The nanoparticles are calcined in air at 573 K.

Paper

processus, dissociating the "event" and defining the number of incident photons responsible for the photocatalytic process are complex matters.[5] According to the quantum yield introduced by Serpone for homogeneous photocatalysis,[5] photocatalytic efficiency (eqn (2)) is defined simply by the number of given events (mineralization, molecules photoconverted or radicals production) relative to the total number of photons incident on the reactor wall. In this work, the photocatalytic efficiency Φ indicates the number of molecules degraded divided by the number of incident photons absorbed by the reactant(s) or by the photocatalysts for all of the irradiation. Thus,

$$\Phi = \frac{N_A \times V \times \Delta c}{I \times S \times \Delta t} \tag{2}$$

where N_A is the Avogadro constant (mol^{-1}), V the volume of the photoreactor (l), Δc the difference between the initial and the final concentration ($mol\ l^{-1}$), I the flux density measured at the surface of the reactor (number of photons $m^{-2}\ s^{-1}$), Δt the irradiation time (s) and S the receptor surface (m^2). The measured photons on the reactor represent the efficient photons received under solar irradiation in the spectral range from 250 to 1000 nm.[35] The photocatalytic efficiencies measurements were replicated a minimum of three times on each sample.

3.2.1. Effect of the precursor content.

A first study has been performed on the influence of the calcium content on the photocatalytic efficiencies of $Zn_{1-x}Ca_xO$ nanoparticles elaborated with a $CaCl_2$ precursor at different compositions ranging from $x = 0.01$ to $x = 0.20$. Fig. 7 represents the variation of photoconverted molecules as a function of the number of photons received in the spectral range from 250 to 700 nm. The slopes of these lines correspond to the photocatalytic efficiency of each catalyst. Fig. 7 shows that the nanoparticles are photosensitive under solar irradiation. In that case, the photocatalytic efficiency decreases with increasing calcium content.
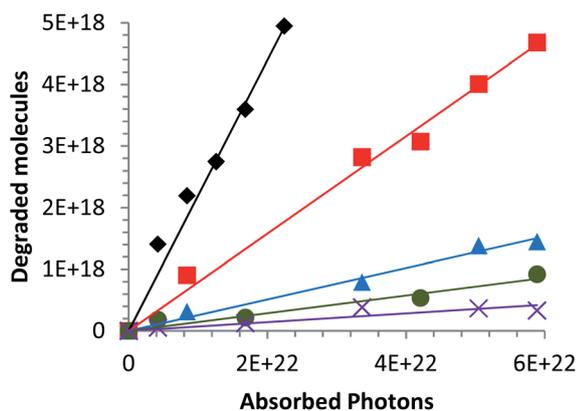
This is due to the increase of the secondary phases present in the material and identified in part 3.1 (Fig. 6d). According to Linder *et al.*, inorganic ions such as Cl^- can be harmful to the photocatalyst efficiency.[59] The optimal alloy percentage for the $CaCl_2$ precursor is 1%. The performance of these nanoparticles is now compared to those of the nanoparticles elaborated with the other precursors.

3.2.2. Effect of the precursor nature.

In second part, the variation of the photocatalytic efficiency under solar irradiation of $Zn_{1-x}Ca_xO$ nanoparticles elaborated with different precursors and with x varying from 0 to 0.20 is shown in the Fig. 8. For all precursors, the photocatalytic efficiency was directly deduced as from eqn (2). As it can be seen from this graph, the photocatalytic results vary drastically depending upon the precursor used. $Zn_{1-x}Ca_xO$ nanoparticles elaborated with a $CaCO_3$ and a $CaSO_4$ precursors present similar trends. On one hand, their photocatalytic efficiencies increase with increasing calcium content, reaching a maximum at $x = 0.10$ and exhibiting a plateau for the $CaSO_4$ precursor after that, whereas for the $CaCO_3$ precursor the efficiency decreases when the calcium content is further increased.

On the other hand, for the two other precursors an increase of calcium content tends to decrease the photocatalytic efficiency. In this case, the decrease is more rapid with a $CaCl_2$ precursor. Compared to undoped ZnO, the Ca-alloyed ZnO elaborated with a $CaCO_3$ precursor enhances the photocatalytic performances. It's important to note that the photocatalytic efficiency is multiplied by a factor of 2. In the case of the $CaSO_4$ precursor, the photocatalytic efficiency stays close to that of undoped ZnO. In contrast, the nanoparticles elaborated using the two others precursors, $CaCl_2$ and $Ca(NO_3)_2$, exhibit similar or even worse photocatalytic results than undoped ZnO.

Two key parameters have thus been identified as responsible for the evolution of the photocatalytic performances. The first is the choice of the precursor and the second is the Ca content used for a given precursor. The enhancement of the photocatalytic efficiency for the $Zn_{1-x}Ca_xO$ nanoparticles elaborated with

Fig. 7 Variation in the number of degraded molecules as a function of the number of absorbed photons in the ultraviolet and visible spectral range (250–700 nm) for different catalysts elaborated with a $CaCl_2$ in suspension: (♦) $Zn_{0.99}Ca_{0.01}O$, (■) $Zn_{0.95}Ca_{0.05}O$, (▲) $Zn_{0.90}Ca_{0.10}O$, (●) $Zn_{0.85}Ca_{0.15}O$ and (✕) $Zn_{0.80}Ca_{0.20}O$. The Ca-alloyed ZnO samples are calcined in air at 573 K.
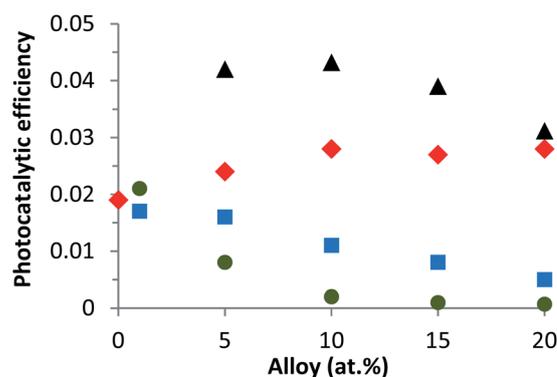
Fig. 8 Variation of the photocatalytic efficiency as a function of the alloy content from the UV and visible spectral range (250–700 nm) for different catalysts calcined in air at 573 K in suspension: (▲) $Zn_{1-x}Ca_xO$ with a $CaCO_3$ precursor, (♦) $Zn_{1-x}Ca_xO$ with a $CaSO_4$ precursor, (■) $Zn_{1-x}Ca_xO$ with a $Ca(NO_3)_2$ precursor and (●) $Zn_{1-x}Ca_xO$ with a $CaCl_2$ precursor.

a $CaCO_3$ precursor at x ranging from 0.05 to 0.20 is due to the Ca^{2+} ions substituting the Zn interstitial sites of the ZnO matrix. The possible explanation could be that during ZnO doping, enhancements of the photocatalytic activity, by an increase of the dopant content, present as a band gap decrease, leads to an effective lower energy photons absorption. As shown in our previous study, the Ca-doped ZnO presents a lower band gap than the pristine ZnO that is to say, an increase of the absorption to the lower wavelength.[60] Moreover, the doping created trapping sites which affects the charges carrier lifetime. In this sense, charge recombinations are reduced and lead to a best photocatalytic efficiency.[2,3,61,62] On the contrary, when higher dopant content is reached, a multiple trapping of charges carriers appears. This leads to an increase of the possibly of the electron–hole recombination and decrease charge carriers which reach the surface to initiate the degradation of molecule, hence decrease of the photocatalytic efficiency.[63,64] The $Zn_{1-x}Ca_xO$ catalyst at $x = 0.10$ elaborated with a $CaCO_3$ precursor provides the best photocatalytic efficiency. For the $Zn_{1-x}Ca_xO$ nanoparticles elaborated with a $CaSO_4$ precursor, the photocatalytic efficiency is close to that of undoped ZnO because the calcium isn't integrated in the ZnO matrix as shown in Table 1, Fig. 5b2 and 6b. In contrast, the decrease of the photocatalytic efficiency for the two others precursors is due to the presence of secondary phases in the material identified in Fig. 5c1 and d1, Fig. 6c and d. These phases not only belong to the precursor but they are due to the creation of zinc hydroxyl compound. Linder *et al.* have shown that the inorganic Cl^- and NO_3^- ions degrade the photocatalytic performances.[59] These results are in agreement with those from EDS, XRD and Raman spectroscopy presented in part 3.1.

3.2.3. Correlation between intrinsic defects and photocatalytic efficiency. In order to understand the difference in term of photocatalytic efficiency for these different precursors a correlation between the intrinsic default of the nanoparticles and the photocatalytic efficiency has been done. To take the analysis further, the X-band EPR method at room temperature has been chosen to study and quantify the intrinsic defects in the undoped ZnO and $Zn_{1-x}Ca_xO$ with $x = 0.10$ elaborated with the three precursors ($CaSO_4$, $CaCO_3$ and $CaCl_2$). On the EPR spectra of $Zn_{0.90}Ca_{0.10}O$ elaborated with the cited precursors, it appears that the nanoparticles present two groups of signals that can be assigned to different defects centers. The first is around $g \sim 1.96$ and the second is around $g \sim 2.00$. However, these two signals appear simultaneously with a $CaCl_2$ precursor and only one signal is there for the $CaSO_4$ and the $CaCO_3$ precursors. The signal at $g \sim 1.96$ originates from defects in the bulk (core), whereas the signal near $g \sim 2.00$ arises from surface defects (shell).[65] The main origin of intrinsic defect centers and their assignment are still controversial in the literature and have been so for decades. However, recently core–shell defects have been identified such as negatively charged zinc vacancies (V_{Zn}^-) acting as shallow acceptor and positively charged oxygen vacancies (V_O^+) acting as deep donor, respectively.[66] Supplementary resonance lines are observed for all the nanoparticles elaborated and the lack of information concerning EPR lines in the literature didn't allow us to identify them. We strongly believe that this line belongs to the precursor used during the

synthesis as we demonstrated in part 3.1. On the other hand, for the $Zn_{0.90}Ca_{0.10}O$ catalyst elaborated with a $CaCl_2$ precursor the asymmetry of the sextuplet signal is associated to the chlorine isotopes ^{35}Cl and ^{37}Cl with $I = 3/2$.[67] This result corroborates with those obtained by EDS, XRD and Raman spectroscopy. Having identified these defects, we have quantified the number of defects present in our nanoparticles of undoped ZnO and $Zn_{1-x}Ca_xO$ elaborated with a $CaSO_4$, a $CaCO_3$ and a $CaCl_2$ precursor at $x = 0.10$. To this end it is important to note that the surface of spectra obtained from the derivative of the EPR absorption as a function of the magnetic field is directly related to the spin number N_s in the sampled material. The spin number is calculated experimentally from the integral of the derivative signal of absorption and from the standard sample whose spin number is known.

The number of defects is estimated using the following eqn (3).[68]

$$N_s = \frac{S}{S_0} \times \left(\frac{SW}{SW_0}\right)^2 \times \frac{G_0}{G} \times N_0 \qquad (3)$$

where N_s is the number of defects, S the surface of the integrated signal, SW the sweep width (Gauss) and G the gain. The subscript "0" refers to spin number, integral and other conditions used with DPPH. It should be noted that this comparative method requires spectra acquisition under the same conditions of power and amplitude modulation as the standard one. The spin number (N_s) is then reported at its mass (spins g^{-1}). The number of defects core, shell and other of undoped ZnO and $Zn_{0.90}Ca_{0.10}O$ nanoparticles elaborated with a $CaSO_4$, a $CaCO_3$ and a $CaCl_2$ precursor are reported in the Fig. 9. On this same figure is also reported the photocatalytic efficiency under solar irradiation in order to correlate it with the number of defects.

In Fig. 9, a drastic increase of the number of defects can be observed when using the $CaCl_2$ precursor. However, the two others precursors caused the number of defects to decrease in comparison with the undoped ZnO. The absence of core defects as well as a low quantity of total defects in the catalysts present the best photocatalytic efficiency. On the other hand, a huge presence of core defects in the $Zn_{0.90}Ca_{0.10}O$ nanoparticles elaborated with a $CaCl_2$ precursor decrease drastically the photocatalytic efficiency.

The best photocatalytic efficiency is obtained for the $Zn_{0.90}Ca_{0.10}O$ nanoparticles elaborated with a $CaCO_3$ precursor. It is important to notice that the core–shell defects in the material play an essential role on the photocatalytic efficiency. The presence of core defects is attributed to negatively charged zinc vacancies representing electron traps, which facilitate charges recombination. The presence of those defects has a harmful effect in photocatalysis. This is also the case for the presence of other defect attributed to Cl^- ions in the synthesis using a $CaCl_2$ precursor.[59] The nature of the precursor clearly influences the type and the number of defects on the synthesized catalysts. The synthesis of catalysts with a controlled density of defects is essential to enhance catalysts performances. Therefore, a future study will be done by annealing nanoparticles in a controlled atmosphere such as O_2, H_2 or N_2.
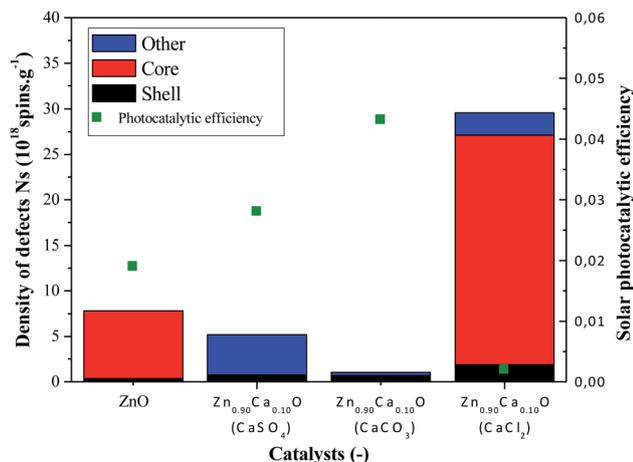
Fig. 9 Variation of the density of defects and photocatalytic efficiency under solar irradiation for undoped ZnO and $Zn_{0.90}Ca_{0.10}O$ nanoparticles with a $CaSO_4$, a $CaCO_3$ and a $CaCl_2$ precursor: (■) number defects in the core, (■) number of defects at the surface (shell), (■) other defects and (■) photocatalytic efficiency under solar irradiation.

4. Conclusions

$Zn_{1-x}Ca_xO$ nanoparticles elaborated with four calcium precursors ($CaSO_4$, $CaCO_3$, $Ca(NO_3)_2$ and $CaCl_2$) with x ranging from 0 to 0.20 have been synthesized by the sol–gel process followed by supercritical drying and have been used as catalyst in photodegradation mechanism of pyrimethanil. The photocatalytic efficiency has been determined, in order to discriminate between these catalysts.

The aim was to study the influence of the calcium precursor on the photocatalytic efficiencies under solar irradiation, taking into account the overall available photons. The photocatalytic results have shown that the $Zn_{1-x}Ca_xO$ nanoparticles elaborated with a $CaCO_3$ precursor at x ranging from 0 to 0.20 enhance the photocatalytic efficiency under solar irradiation, whereas in the case of the $CaSO_4$ precursor the photocatalytic efficiency is similar to that of ZnO. On the other hand, for the nanoparticles elaborated with the two other precursors the photocatalytic efficiency is degraded. The experimental results obtained in this study lead to the conclusion that the precursor and the calcium content play an essential role on the photocatalytic efficiency.

Characterization of the alloys using a number of complementary techniques shows that only in the case of $Zn_{1-x}Ca_xO$ nanoparticles elaborated with the $CaCO_3$ precursor, calcium ions substituted the zinc interstitial sites in the ZnO matrix. In contrast, for the three other precursors, the presence of secondary phases in the catalyst and the similarly of the lattice parameters in comparison to ZnO indicates that the calcium isn't introduced in the ZnO matrix. Moreover, the number of intrinsic defects in the material decreased when the $CaCO_3$ precursor was used. It is shown that a substantial density of total defects (core, shell and other defects) induces a drastic decrease of the catalysts photocatalytic efficiency. In this work, it has been demonstrated that the presence of core defects in the material is harmful in photocatalysis due to electrons–holes charges recombination.

The maximal photocatalytic efficiency has been obtained for $Zn_{1-x}Ca_xO$ nanoparticles elaborated with a $CaCO_3$ precursor at $x = 0.10$, for which we have confirmed the disappearance of core defects and a low presence of shell and other defects. These results are promising for the development of new high-performance photocatalysts.

Conflicts of interest

There are no conflicts to declare.

Acknowledgements

References

1 J. Galvez and S. Malato Rodriguez, *Solar Detoxification*, United Nations Educ. Sci. Cult. Organ., 2003, p. 237.

2 A. L. Linsebigler, G. Lu and J. T. Yates, *Chem. Rev.*, 1995, **95**, 735–758.

3 M. R. Hoffmann, S. T. Martin, W. Choi and D. W. Bahnemannt, *Chem. Rev.*, 1995, **95**, 69–96.

4 S. Malato, J. Blanco, J. Cáceres, A. R. Fernández-Alba, A. Agüera and A. Rodríguez, *Catal. Today*, 2002, **76**, 209–220.

5 N. Serpone, *J. Photochem. Photobiol., A*, 1997, **104**, 1–12.

6 J. M. Herrmann, *Top. Catal.*, 2005, **34**, 49–65.

7 G. Plantard, F. Correia and V. Goetz, *J. Photochem. Photobiol., A*, 2011, **222**, 111–116.

8 M. Faisal, A. A. Ismail, A. A. Ibrahim, H. Bouzid and S. A. Al-Sayari, *Chem. Eng. J.*, 2013, **229**, 225–233.

9 N. C. S. Selvam, S. Narayanan, L. J. Kennedy and J. J. Vijaya, *J. Environ. Sci.*, 2013, **25**, 2157–2167.

10 R. Daghir, P. Drogui and D. Robert, *Ind. Eng. Chem. Res.*, 2013, **52**, 3581–3599.

11 D. B. Hernandez-Uresti, D. Sánchez-Martínez, A. Martínez-De La Cruz, S. Sepúlveda-Guzmán and L. M. Torres-Martínez, *Ceram. Int.*, 2014, **40**, 4767–4775.

12 A. Dodd, A. McKinley, M. Saunders and T. Tsuzuki, *Nanotechnology*, 2006, **17**, 692–698.

13 N. Soltani, E. Saion, W. Mahmood Mat Yunus, M. Navasery, G. Bahmanrokh, M. Erfani, M. R. Zare and E. Gharibshahi, *Sol. Energy*, 2013, **97**, 147–154.

14 Y. L. Min, G. Q. He, Q. J. Xu and Y. C. Chen, *J. Mater. Chem. A*, 2014, **2**, 2578–2584.

15 D. P. Mohapatra, S. K. Brar, R. Daghrir, R. D. Tyagi, P. Picard, R. Y. Surampalli and P. Drogui, *Sci. Total Environ.*, 2014, **485–486**, 263–269.

16 J. M. Herrmann, *Catal. Today*, 1999, **53**, 115–129.

17 A. Carabin, P. Drogui and D. Robert, *J. Taiwan Inst. Chem. Eng.*, 2015, **54**, 109–117.

18 I. Poulios, D. Makri and X. Prohaska, *Global NEST J.*, 1999, **1**, 55–62.

19 S. Anandan, A. Vinu, T. Mori, N. Gokulakrishnan, P. Srinivasu, V. Murugesan and K. Ariga, *Catal. Commun.*, 2007, **8**, 1377–1382.

20 M. Romero, J. Blanco, B. Sánchez, A. Vidal, A. I. Cardona and E. Garcia, *Sol. Energy*, 1999, **66**, 169–182.

21 H. J. Lee, J. H. Kim, S. S. Park, S. S. Hong and G. D. Lee, *J. Ind. Eng. Chem.*, 2015, **25**, 199–206.

22 F. Barka-Bouaifel, B. Sieber, N. Bezzi, J. Benner, P. Roussel, L. Boussekey, S. Szunerits and R. Boukherroub, *J. Mater. Chem.*, 2011, **21**, 10982.

23 M. Fu, Y. Li, S. Wu, P. Lu, J. Liu and F. Dong, *Appl. Surf. Sci.*, 2011, **258**, 1587–1591.

24 R. Saleh and N. F. Djaja, *Spectrochim. Acta, Part A*, 2014, **130**, 581–590.

25 N. Serpone, D. Lawless, J. Disdier and J.-M. Herrmann, *Langmuir*, 1994, **10**, 643–652.

26 N. I. Al-Salim, S. A. Bagshaw, A. Bittar, T. Kemmitt, A. James McQuillan, A. M. Mills and M. J. Ryan, *J. Mater. Chem.*, 2000, **10**, 2358–2363.

27 H. Benhebal, M. Chaib, A. Leonard, S. D. Lambert and M. Crine, *Mater. Sci. Semicond. Process.*, 2012, **15**, 264–269.

28 W. Choi, A. Termin and M. R. Hoffmann, *J. Phys. Chem.*, 1994, **98**, 13669–13679.

29 A. G. Agrios and P. Pichat, *J. Appl. Electrochem.*, 2005, **35**, 655–663.

30 U. I. Gaya and A. H. Abdullah, *J. Photochem. Photobiol., C*, 2008, **9**, 1–12.

31 K. Djessas, I. Bouchama, J. L. Gauffier and Z. Ben Ayadi, *Thin Solid Films*, 2014, **555**, 28–32.

32 European Food Safety Authority, *EFSA J.*, 2011, **9**, 65.

33 J. M. Gerage, A. P. G. Meira and M. V. da Silva, *Nutrire*, 2017, **42**, 3.

34 I. Bernabò, A. Guardia, R. Macirella, S. Sesti, A. Crescente and E. Brunelli, *Aquat. Toxicol.*, 2016, **172**, 56–66.

35 A. Rosset, G. Plantard, K. Djessas and V. Goetz, *J. Mater. Sci.: Mater. Electron.*, 2017, **28**, 8739–8748.

36 H. E. Swanson, *Standard X-ray diffraction powder patterns*, 1953, vol. 1–22, pp. 24–30.

37 C. G. Kontoyannis and N. V. Vagenas, *Analyst*, 1999, **125**, 251–255.

38 H. F. McMurdie, M. C. Morris, E. H. Evans, B. Paretzkin and W. Wong-Ng, *Powder Diffr.*, 1986, **1**, 265–275.

39 E. H. E. Marlene, C. Morris, H. F. McMurdie, N. C. P. Boris Paretzkin and H. S. Parker, *Standard X-Ray Diffraction Powder Patterns I*, 1981, vol. 539.

40 H. Chen, L. Zhu, H. Liu and W. Li, *Electrochim. Acta*, 2013, **105**, 289–298.

41 R. Dhahri, M. Hjiri, L. El Mir, E. Fazio, F. Neri, F. Barreca, N. Donato, A. Bonavita, S. G. Leonardi and G. Neri, *J. Phys. D: Appl. Phys.*, 2015, **48**, 255503.

42 H. Saeki, H. Tabata and T. Kawai, *Solid State Commun.*, 2001, **120**, 439–443.

43 S. Kolesnik, B. Dabrowski and J. Mais, *J. Appl. Phys.*, 2004, **95**, 2582–2586.

44 S. Ramachandran, J. Narayan and J. T. Prater, *Appl. Phys. Lett.*, 2006, **88**, 1–4.

45 B. D. Cullity, *Elements of X-ray diffraction*, Addison-Wesley, Reading, 1978, p. 102.

46 T. C. Damen, S. P. S. Porto and B. Tell, *Phys. Rev.*, 1966, **142**, 1085–1333.

47 J. Calleja and M. Cardona, *Phys. Rev. B: Solid State*, 1977, **16**, 3753–3761.

48 R. Cuscó, E. Alarcón-Lladó, J. Ibanez, L. Artús, J. Jiménez, B. Wang and M. J. Callahan, *Phys. Rev. B: Condens. Matter Mater. Phys.*, 2007, **75**, 165202.

49 S. Singh and M. S. R. Rao, *Phys. Rev. B: Condens. Matter Mater. Phys.*, 2009, **80**, 045210.

50 A. Umar, S. H. Kim, Y. S. Lee, K. S. Nahm and Y. B. Hahn, *J. Cryst. Growth*, 2005, **282**, 131–136.

51 Y. J. Xing, Z. H. Xi, Z. Q. Xue, X. D. Zhang, J. H. Song, R. M. Wang, J. Xu, Y. Song, S. L. Zhang and D. P. Yu, *Appl. Phys. Lett.*, 2003, **83**, 1689–1691.

52 B. J. Berenblut, P. Dawson and G. R. Wilkinson, *Spectrochim. Acta, Part A*, 1973, **29**, 29–36.

53 D. E. Irish and G. E. Walrafen, *J. Chem. Phys.*, 1967, **46**, 378.

54 H. Marchebois, S. Joiret, C. Savall, J. Bernard and S. Touzain, *Surface and Coatings Technology*, 2002, **157**, 151–161.

55 N. S. Azmat, K. D. Ralston, B. C. Muddle and I. S. Cole, *Corros. Sci.*, 2011, **53**, 1604–1615.

56 R. Autengruber, G. Luckeneder and A. W. Hassel, *Corros. Sci.*, 2012, **63**, 12–19.

57 M. Khatamian, A. A. Khandar, B. Divband, M. Haghighi and S. Ebrahimiasl, *J. Mol. Catal. A: Chem.*, 2012, **365**, 120–127.

58 R. Saleh and N. F. Djaja, *Superlattices Microstruct.*, 2014, **74**, 217–233.

59 M. Lindner, D. W. Bahnemann, B. Hirthe and W.-D. Griebler, *J. Sol. Energy Eng.*, 1997, **119**, 120–125.

60 A. Rosset, G. Plantard and K. Djessas, *J. Environ. Chem. Eng.*, 2018, **6**, 7273–7283.

61 K. Umar, M. M. Haque, M. Muneer, T. Harada and M. Matsumura, *J. Alloys Compd.*, 2013, **578**, 431–438.

62 K. Umar, A. Aris, T. Parveen, J. Jaafar, Z. Abdul Majid, A. Vijaya Bhaskar Reddy and J. Talib, *Appl. Catal., A*, 2015, **505**, 507–514.

63 K. Wilke and H. D. Breuer, *J. Photochem. Photobiol., A*, 1999, **121**, 49–53.

64 J. Liqiang, S. Xiaojun, X. Baifu, W. Baiqi, C. Weimin and F. Honggang, *J. Solid State Chem.*, 2004, **177**, 3375–3382.

65 P. Jakes and E. Erdem, *Phys. Status Solidi*, 2011, **5**, 56–58.

66 S. K. S. Parashar, B. S. Murty, S. Repp, S. Weber and E. Erdem, *J. Appl. Phys.*, 2012, **111**, 113712.

67 D. Suryanarayana and J. Sobhanadri, *J. Magn. Reson.*, 1974, **16**, 274–282.

68 B. Demirboğa and a. M. Önal, *J. Phys. Chem. Solids*, 2000, **61**, 907–913.